Received: 11 February 2019 | Revised: 17 January 2020 | Accepted: 23 January 2020
DOI: 10.1002/we.2486

WILEY

RESEARCH ARTICLE

An experimental study on the effects of winglets on the tip vortex interaction in the near wake of a model wind turbine

Franz Mühle[1,2] | Jan Bartl[3] | Thomas Hansen[4] | Muyiwa Samuel Adaramola[1] | Lars Sætran[5]

[1]Faculty of Environmental Sciences and Natural Resource Management, Norwegian University of Life Sciences, Ås, Norway
[2]Chair of Wind Energy, Technical University of Munich, München, Germany
[3]Department of Mechanical and Marine Engineering, Western Norway University of Applied Sciences, Bergen, Norway
[4]Bergen Offshore Wind Center, Geophysical Institute, University of Bergen, Bergen, Norway
[5]Department of Energy and Process Engineering, Norwegian University of Science and Technology, Trondheim, Norway

Correspondence
Jan Bartl, Department of Mechanical and Marine Engineering, Western Norway University of Applied Sciences, Inndalsveien 28, N-5063 Bergen, Norway.
Email: jan.bartl@hvl.no

Abstract

An experimental study of the near wake up to four rotor diameters behind a model wind turbine rotor with two different wing tip configurations is performed. A straight-cut wing tip and a downstream-facing winglet shape are compared on the same two-bladed rotor operated at its design tip speed ratio. Phase-averaged measurements of the velocity vector are synchronized with the rotor position, visualizing the downstream location of tip vortex interaction for the two blade tip configurations. The mean streamwise velocity is found not to be strongly affected by the presence of winglet tip extensions, suggesting an insignificant effect of winglets on the time-averaged inflow conditions of a possible downstream wind turbine. An analysis of the phase-averaged vorticity, however, reveals a significantly earlier tip vortex interaction and breakup for the wingletted rotor. In contradistinction, the tip vortices formed behind the reference configuration are assessed to be more stable and start merging into larger turbulent structures significantly further downstream. These results indicate that an optimized winglet design can not only contribute to a higher energy extraction in a rotor's tip region but also can positively affect the wake's mean kinetic energy recovery by stimulating a faster tip vortex interaction.

KEYWORDS

tip vortex, wake, wind energy, winglets

1 | INTRODUCTION

Winglets are small extensions at the tip of any kind of lift-generating wing of finite length. Best known from their widespread application in modern aviation, winglets are recognized to reduce induced drag in the tip regions of aircraft wings. Several studies confirmed a reduction in induced drag leading to a significant decrease in fuel consumption of modern transportation airplanes (eg, van Dam et al,[1] Eppler,[2] and Faye et al[3]). The formation of a tip vortex occurs at any kind of tip shape of a loaded wing due to a secondary flow from the wing's pressure to its suction side around the tip. The spanwise flow in the tip region reduces the local angle of attack and induces additional drag near the tip (Giuni and Green[4]). Although winglets cannot suppress the formation of a tip vortex, they might be able to modify the strength and shape of the tip vortex. When applying winglets on a wind turbine rotor, positive effects on the rotor's performance as well as the breakup mechanisms of the tip vortices in the wake are desirable.

Most of the research related to the application of winglets on wind turbines focused on the optimization of an individual rotor's performance. Johansen and Sørensen[5] designed six different winglet shapes for wind turbine rotors and simulated the flow around the blade tips. Their results confirmed that good winglet designs are able to improve a rotor's power coefficient by around 1.0% and can decrease its performance if poorly designed. In a follow-up study, Johansen and Sørensen[6] optimized the winglet's geometry parameters and found a rotor power increase of 2.6%. Another study by Gaunaa and Johansen[7] showed a stronger positive effect on the power coefficient for downstream-facing winglets than

The peer review history for this article is available at https://publons.com/publon/10.1002/we.2486

for upstream-facing winglets. A free-wake vortex analysis method was used by Maniaci and Maughmer (2012) for the design of rather large downstream-facing winglets with a height of 8% of the rotor radius. They simulated an increase in power coefficient of 9% and thus confirmed the large influence of the winglet's height on the performance. The same rotor was also used by Gertz et al,[8] who experimentally tested different winglet designs and found performance increases between 5% and 8%. An optimization algorithm was used by Hansen and Mühle[9] to design the winglets for the model scale turbine, which is also investigated in the present study. The winglet's geometry parameters were optimized for a maximum power coefficient at the turbine's design tip speed ratio. The final winglet geometry was the result of an optimization procedure using a Kriging surrogate model. The power and thrust force was obtained through a Reynolds-averaged Navier-Stokes simulation using a Spalart-Allmaras turbulence model. Numerical predictions and a wind tunnel validation of the rotor performance found a power increase of 7.8% and 10.3%, respectively, compared with a nonwingletted reference rotor. A smaller number of recent studies also focused on the wake flow behind a wind turbine with winglets, investigating which effect the tip extensions could have on a cluster of multiple turbines. A recent experiment by Ostovan and Uzol[10] compared the performance of a two-turbine array with and without winglets attached to the blade tips of the upstream turbine ($D = 0.90$ m). They measured an increase of about 2.5% in the upstream turbine's power production. Although winglets attached to the upstream turbine caused a smaller energy production on an aligned downstream turbine, the combined efficiency of both turbines was still found to increase for the wingletted configuration. The focus was shifted on the very near wake behind the rotor in a follow-up study by Ostovan et al,[11] in which they used Particle-Image-Velocimetry (PIV) to measure the tip vortex strength in the near wake for a wingletted and a straight-cut blade tip configuration. It was shown that the core vorticity levels were significantly smaller for the wingletted configuration, while the vortex core diameter was measured to be larger. The mixing layer thickness was observed to be higher for the winglet case. An analysis of the streamwise velocity showed a wider wake extension for the wingletted configuration. Another PIV study of the wake up to $x/D = 5$ behind a significantly smaller rotor of $D = 0.12$ m with and without winglets was conducted by Tobin et al.[12] Their PIV study indicated an increased velocity deficit in the wake of the wingletted rotor. Although another downstream turbine, which was operated in the wake, was found to produce less power, the combined power of the two-turbine array could be increased by the use of winglets. Interestingly, their results furthermore indicated a similar level of tip vortex circulation for the wingletted and baseline rotor. Although both instantaneous and phase-averaged quantities were measured by Tobin et al,[12] no analysis on the effect of winglets on the breakup mechanisms of the tip vortices was presented. The stability of the tip vortices in the wake of a wind turbine rotor is currently a widely discussed research topic (Sørensen,[13] Sarmast et al,[14] and Okulov et al[15]). The vortices shed from the blade tips form a helical vortex system in the near-wake behind a rotor. At some point, the individual vortex spirals start to interact, break up, and merge into turbulent structures. The vortex stability in the near wake determines the initial conditions for the far wake behind a wind turbine, which itself is crucial to correctly predict wake-turbine interactions in wind farms. An experimental PIV study of the vortex interaction in the wake up to $x/D = 5$ behind a two-bladed model turbine of $D = 0.60$ m was performed by Lignarolo et al.[16] Their results emphasized the importance of the wake instability caused by a pairwise interaction of the tip vortices on the momentum deficit in the wake, which was shown to be strongly dependent on the turbine's tip speed ratio. An analysis of the development of the turbulent stresses in the wake demonstrated a strong influence of the vortex interaction on a more effective wake mixing after the location of the initial instability. A further experimental study on the transition from coherent to turbulent motions in the wake of a three-bladed model wind turbine was performed by Eriksen and Krogstad.[17] Using phase-averaging on the three-dimensional velocity vector acquired from hot-wire anemometry, they found that the wake is dominated by coherent motions up to $x/D = 1$ before the vortices start to interact. The mutual induction of two of the three tip vortices was observed to be fully developed by $x/D = 2$, gradually merging into larger turbulent structures. By $x/D = 3$, the flow field was seen to be dominated by turbulent motions. Another extensive PIV study of the wake behind a small rotor of $D = 0.12$ m with straight wing tips was reported by Bastankhah and Porté-Agel[18] for different turbine tip speed ratios. They found stronger and more stable tip vortices for the optimal tip speed ratio than for the significantly higher run-away tip speed ratio. Because of the small size of the rotor with respect to turbulent length scales in the inflow, meandering motions of the wake were observed in this experiment, not making it possible to use phase-averaged wake properties to identify the locations of tip vortex breakup. The objective of the present study is to investigate how optimized winglets attached to a model turbine's blade tips affect the recovery of the wake flow behind it. Conservation of energy would suggest a lower kinetic energy level in the wake due to a higher energy extraction of the wingletted rotor. However, this simplified consideration does not take a possibly modified interaction and break up of the tip vortices into account, which is governing the entrainment of high-energy freestream fluid from outside of the wake. For this purpose, highly spatially resolved measurements in cross-flow direction are performed in the wake behind a two-bladed rotor with winglets and the same reference rotor blade with straight-cut tips. By an analysis of the phase-averaged quantities, we investigate if winglets enhance the breakup of the tip vortices and possibly promote the recovery process of the wake velocity deficit. A decomposition of the time-averaged turbulent stresses in the wake will furthermore describe how the production of turbulence is modified by the presence of winglets at the blade tips.

2 | SETUP AND METHODS

2.1 | Model wind turbine rotor

As shown in Figure 1, a two-bladed rotor with a total diameter of $D = 0.90$ m with attachable blade tips is applied for the experiments. A custom designed airfoil *R-opt* is used along the entire blade span, while another optimized airfoil shape *W-opt* is used for the winglets; see Hansen and Mühle.[9]

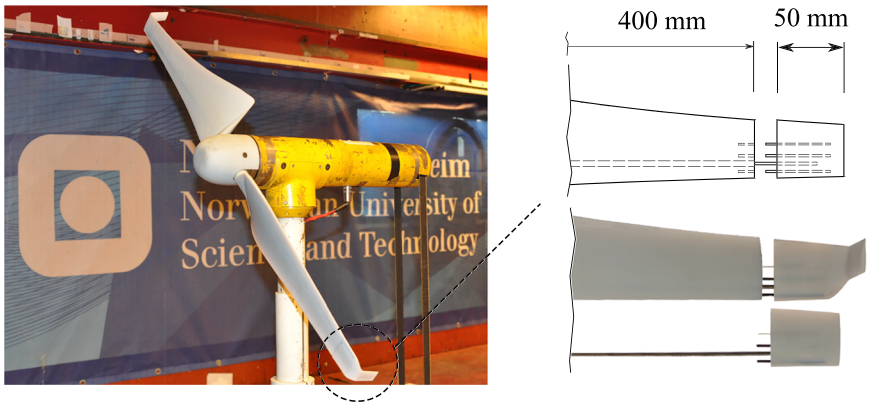

FIGURE 1 Rotor with exchangeable wingtips [Colour figure can be viewed at wileyonlinelibrary.com]

TABLE 1 Winglet design variables

Parameters	Value	Reference
Span	10.76%	Rotor span
Sweep	17.86°	-
AoA	-1.17°	-
Radius	3.09%	Rotor span
Root chord	58%	Rotor tip chord
Tip chord	88%	Winglet root chord

The blade tips are exchangeable through a seamless joint located 50 mm from the tip. Two sets of blade tips can be attached, the first of which is a straight-cut blade tip (reference configuration) with a tip chord length of $L_{c,tip} = 39.7$ mm. The second tip configuration is a downstream-facing winglet, the main geometry parameters of which are summarized in Table 1. The operational characteristics of both rotor configurations are illustrated in Figure 2. Both rotor configurations have their optimum tip speed ratio slightly above $\lambda = 6.0$, while the wingletted rotor produces significantly more power and experiences higher thrust forces at the design point. The reference rotor has a power coefficient of $C_{P,ref} = 0.468$, which rises to $C_{P,winglets} = 0.518$ for the wingletted tip configuration. Simultaneously, the rotor's thrust coefficient at $\lambda = 6.0$ increases from $C_{T,ref} = 0.870$ to $C_{T,winglets} = 0.980$, when winglets are attached to the blade tips. These values might appear very high compared with full-scale wind turbines but can be explained by a rather high blockage by the wind tunnel boundaries. The rotor swept area blocks about 12.8% of the wind tunnel's cross-sectional area, which affects the flow expansion around the rotor. A numerical study of the blocked and unblocked flow around the rotor has been performed by Hansen and Mühle.[9] The tip speed ratio is fixed to $\lambda = 6.0$ during the entire experiment for both configurations.

2.2 | Wind tunnel and measurement grid

The experiments are performed in the closed-loop wind tunnel at the Norwegian University of Science and Technology (NTNU) in Trondheim, Norway. It has a cross section of 2.71 m (width) × 1.81 m (height) and measures 11.0 m in length. The inflow is spatially uniform and features a turbulence intensity of $TI = 0.23\%$ for an inflow velocity of $U_\infty = 10.0$ m/s, which is chosen for all presented measurements. The wake flow is measured at 18 streamwise measurement locations ranging from $x/D = 0.1$ to $x/D = 4.0$ in the wake downstream of both rotor configurations as shown in Figure 3. At each of those locations, a horizontal line at the turbine's hub height is measured from $z/D = 0$ to $z/D = 0.85$. A total of 76 measurement points are scanned in lateral direction with a varying spatial resolution in the different regions of the wake. In the region around the path of the tip vortex, from $z/D = 0.45$ to $z/D = 0.75$, a very high spatial resolution of $\Delta z = 5$ mm is scanned.

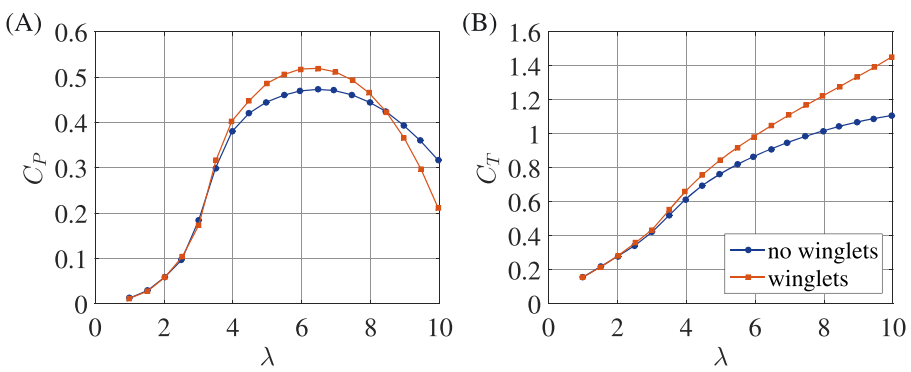

FIGURE 2 A, Power coefficient C_P and B, thrust coefficient C_T of the nonwingletted reference rotor (blue) and wingletted rotor (red) [Colour figure can be viewed at wileyonlinelibrary.com]

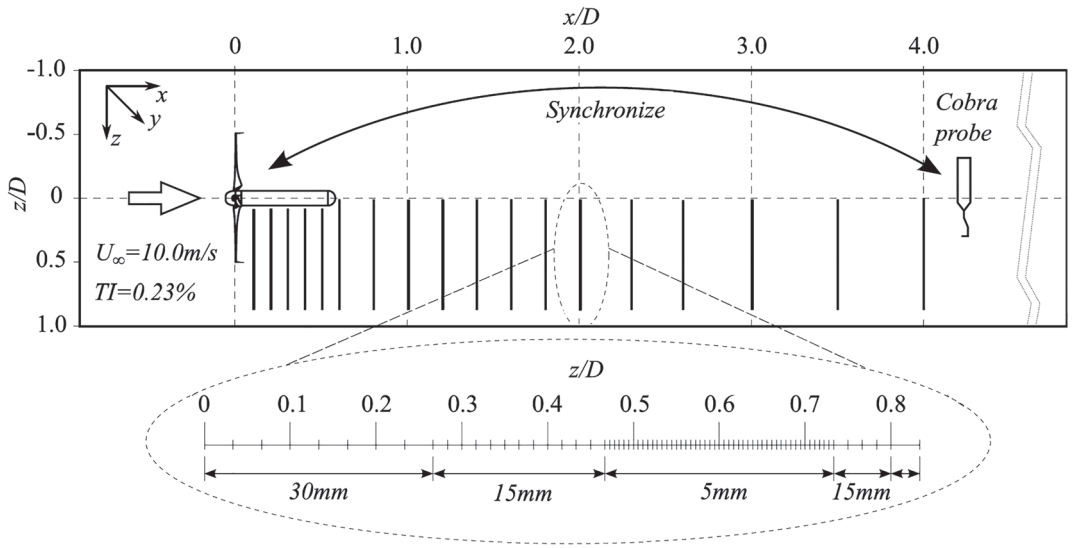

FIGURE 3 Top view of the experimental setup, reference coordinate system, and measurement grid in the wake behind the rotor. The single measurement locations in the zoomed area are representative for all 18 line measurements in the wake[17] [Colour figure can be viewed at wileyonlinelibrary.com]

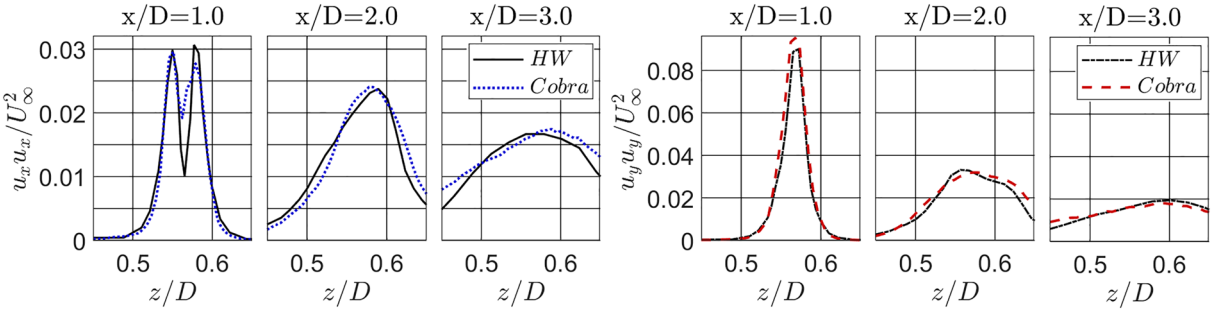

FIGURE 4 Comparison of the normalized normal stress components $u_x u_x/U_\infty^2$ and $u_y u_y/U_\infty^2$ measured with the Cobra probe and a Hot-Wire probe, respectively, at three downstream locations in the wake behind three-bladed NTNU reference rotor. Hot-wire data from Eriksen and Krogstad[17] [Colour figure can be viewed at wileyonlinelibrary.com]

2.3 | Flow measurement techniques

For the measurement of the wake flow, two Cobra probes of the type *Series 100* manufactured by Turbulent Flow Instrumentation (TFI) are applied. A Cobra probe is a four-hole pressure probe, which is able to resolve all three components of the velocity vector. It should be noted that pressure-based measurements are generally not considered to be an established measurement technique for tip vortex dynamics in a wind turbine wake yet. Given the relatively high frequency response ($f_{oversample}$ = 10 000 Hz,) and relatively small probe head diameter (D_{head}=2.6 mm corresponding to about 4% of the tip vortex diameter at x/D = 1.0) the Cobra probe fulfills the main requirements for the presented measurements. In Figure 4, a comparison of Cobra probe measurements with a set of Hot-wire measurements of the turbulent stress tensor in wake of the three-bladed NTNU reference rotor is presented, showing a very good match between the two measurement techniques.

In the presented set of experiments, two Cobra probes are used simultaneously in a parallel setup, which significantly reduces the measurement time. Four individual pressure transducers are installed inside each probe, which all are pre-calibrated by the manufacturer. Detailed information of the calibration process and the transformation from the pressures to the velocities is provided by Shepherd.[19] A major experimental challenge of Cobra probe measurements is to obtain a perfectly horizontal installation of the probes in the wind tunnel. This is achieved by an additional validation of the flow velocities measured in the empty wind tunnel by a simultaneous measurement with a two-component Laser-Doppler Anemometer (LDA) at the same location. Thus, the inclination of the Cobra probes can be manually adjusted until both velocity components feature the smallest deviations. The probe is able to resolve high frequencies of up to 2000 Hz, making it possible to also measure time-varying turbulent velocity components (Hooper and Musgrove[20]). In this experiment, over-sampling is applied to reach a time resolution of 10 000 Hz, which is necessary to also extract phase-averaged turbulent quantities from the flow. The over-sampled time series are adequately filtered for noise during the postprocessing of the data. Moreover, the Cobra probe allows to synchronize the flow measurement with the rotor position, which is employed for the measurement of phase-averaged data in the rotor wake. Each measurement point is sampled for t = 40 seconds, covering approximately 850 full rotations of the rotor, which is considered to be sufficiently long for the extraction of phase averaged data. Four

voltage signals corresponding to the single pressures at the probe tips are acquired, which then are evaluated by a MATLAB routine resorting to the calibration tables provided by the manufacturer. Time series of all three velocity components are obtained after the calibration and used to calculate time-averaged velocity components, flow angles, and the turbulent normal and shear stress components. For the calculation of the phase-averaged quantities in the wake, one full rotor revolution is divided in 120 sectors, each of which covers a sector size of 3°. The Cobra probe is able to measure flow angles up to $\theta = 45^\circ$ according to the manufacturer. Therefore, all measurement samples, in which one of the flow angles is $\theta > 45^\circ$ are excluded from the analysis. The percentages of dismissed data points at the different downstream measurement locations in the wake are listed for both rotor configurations in Table 2. Flow angles $\theta > 45^\circ$ are specifically observed in the very near wake up to $x/D = 1.0$ in the tip vortex region, with a significantly higher percentage for phase-averaged data. For this reason, phase-averaged data are only presented for $x/D \geq 1.0$.

2.4 | Measurement uncertainty

The measurement uncertainty of the mean velocity components is obtained for every measurement point by the means of a combination of precision error and systematic error as proposed by Wheeler and Ganji.[21] For this purpose, a systematic error for the Cobra probe of ±1.9% (1.2% calibration plus 1.5% pressure measurement) is taken into account (Shepherd[19]). The maximum total error in the mean streamwise flow component was obtained at $x/D = 0.1$, amounting to 4.5% of the absolute velocity values. Further downstream, the total error was found to be between 1% and 2%, with slightly higher values in the tip vortex region. The uncertainty in the turbulent quantities measured in the wake is calculated according to the procedures proposed by Benedict and Gould.[22] The uncertainties in the turbulent stresses are found to be higher than the mean flow components, typically ranging between 5% and 8%.

3 | RESULTS

3.1 | Mean streamwise velocity

The near wake behind the model wind turbine is scanned in the *xz*-plane, acquiring all three components of the velocity vector. The time-averaged mean streamwise velocity field in the wake $\overline{U_x}/U_\infty$ behind the two rotors is compared in Figure 5A,B. Note that the dotted vertical lines indicate the actual measurement locations, and a linear interpolation is used in the intermediate spaces for a qualitative description of the mean wake flow. The wake velocity deficit is assessed to have a very similar magnitude for both configurations. The lateral wake extension, however, is seen to be slightly wider for the wingletted configuration. This is illustrated in Figure 5C, showing the mean velocity difference $\Delta\overline{U_x}/U_\infty$ of A and B. The red-colored area behind the rotor tip indicates higher velocities for the reference configuration. This is mainly due to a generally wider wake behind the wingletted rotor. For the downstream distances $x/D = 2.0$ - 3.0, however, another area of large velocity difference is observed further inside. This is due to a local enlargement of the shear layer for the wingletted configuration in this region, as will be explained in more detail in Section 3.3 (the stress tensor). Furthermore, a slight increase in mean velocity is observed for the wingletted configuration in the light blue area at the downstream distances $x/D = 3.5$ and 4.0 and spanwise positions $z/D = 0.5$ - 0.6.

The difference in lateral wake extension is additionally analyzed by the means of a flow visualization around the tip regions as shown in Figure 6. For this purpose, smoke is injected into the flow upstream of the blade tip. The flow is illuminated by a stroboscopic light synchronized with the turbine RPM, visualizing the formation of the tip vortices downstream of the rotor for both tip configurations. It can be observed that the winglet in Figure 6B is slightly bent outwards due to the centrifugal forces acting on it. The vortex formation is therefore assumed to take place at a location slightly further outside, possibly contributing to the wider wake expansion for the wingletted configuration. Apart from this slight spanwise dislocation of the vortex formation, the street of tip vortices shed in both tip configurations seem very similar in the visualized near wake up to $x/D = 1.3$.

TABLE 2 Percentages of dismissed data samples due to flow angles $\theta > 45^\circ$ for all downstream measurement locations $x/D = 0.1$ - 3.0

Dist.	time-averaged		phase-averaged	
x/D	no WL	WL	no WL	WL
0.1	16%	24%	53%	52%
0.4	9%	15%	50%	61%
0.6	10%	15%	15%	43%
1.0	7%	14%	8%	40%
1.4	3%	5%	5%	8%
2.0	< 1%	< 1%	2%	3%
3.0	< 1%	< 1%	1%	2%

Note. Four cases are distinguished: time-average vs phase-averaged flow measurements, as well as the nonwingletted reference case (no WL) and the wingletted rotor configuration (WL).

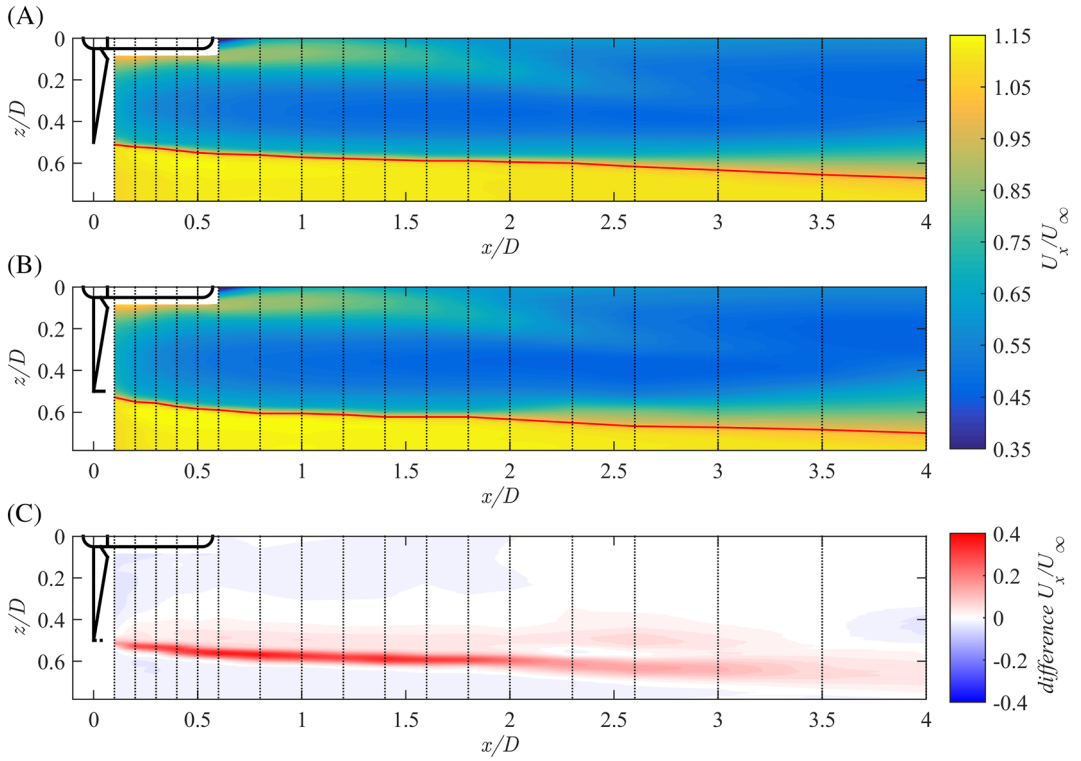

FIGURE 5 Normalized streamwise velocity A, rotor without winglets, B, rotor with winglets, and C, difference between the two rotor concepts (rotor with winglets-rotor without winglets). The red lines indicate locations of $\overline{U_x}/U_\infty = 1$. Dashed vertical lines indicate the downstream measurement locations, while all other values are interpolated [Colour figure can be viewed at wileyonlinelibrary.com]

The effect of winglets on the kinetic energy content in the wake is furthermore investigated by an analysis of the available power of an imaginary downstream rotor, a concept, which is explained in more detail by Bartl et al.[23] The available power is calculated by integrating the velocity profiles at the different downstream distances x/D over a cross section of $r = 0.5D$. In the available power calculation, the wake profile between $z/D = -0.5$ and $z/D = 0.5$ is divided into 20 segments for which the averaged velocity is the integrated according to Equation (1)

$$P = \sum_{i=1}^{20} \rho A_i \langle u_i(t) \rangle_{A_i,t}^3 . \tag{1}$$

Herein, A_i is the ith two-dimensional segment of the wake, and $\langle u_i(t) \rangle$ denotes the temporally and spatially averaged streamwise velocity in the segment A_i. About 5% less power is available for the wingletted configuration for $x/D = 0.5$ - 3.5 as shown in Figure 7, corresponding with the higher energy extraction of the wingletted rotor as previously shown in Figure 2. At a downstream distance of $x/D = 4.0$, however, the available power in the wake of the wingletted rotor is calculated to surpass the kinetic power contained in the wake of the reference rotor. For a better understanding of these effects, the total kinetic energy contained in the shed tip vortices is analyzed in more detail.

3.2 | Total kinetic energy

The total kinetic energy is the sum of the energy contained in the periodic motions of tip vortices and the random turbulent fluctuations $k_{total} = \frac{1}{2}(\overline{\tilde{u}_i \tilde{u}_i} + \overline{u_i' u_i'})$. This triple decomposition method of the time-dependent velocity signal is further described in Cantwell and Coles.[24] The periodic velocity fluctuations are not actually calculated in the present work. The contours of the total kinetic energy in the wake flow are compared for both tip configurations in Figure 8. The total kinetic energy is assessed to be strongest in a small region behind the blade tips in both cases. Directly downstream of the rotor, the tip vortices have not yet interacted and therefore form a path of concentrated kinetic energy up to about $x/D = 2.0$ for both tip configurations. Further, peaks in total kinetic energy are observed behind the blade roots and in the wake of the turbine nacelle. The kinetic energy, however, is seen to quickly decay, and the energy levels are small compared with the tip vortex shear layers in the outer part of the wake. The initial width of the tip vortex paths is measured to be similar for both tip configurations, expanding over an estimated lateral extension of about $\Delta z/D \approx 0.06$. The white lines in Figure 8A,B indicate locations, at which the mean streamwise velocity is equal to the incoming reference velocity $\overline{U_x}/U_\infty = 1$. For both tip configurations, these locations correspond well with the tip vortex trajectories, which create a shear layer between the freestream and the wake flow. From a downstream distance $x/D \geq = 2.0$, significant deviations are detected in the width of the shear layer between the two cases. The shear layer is seen to be significantly broader for the wingletted configuration

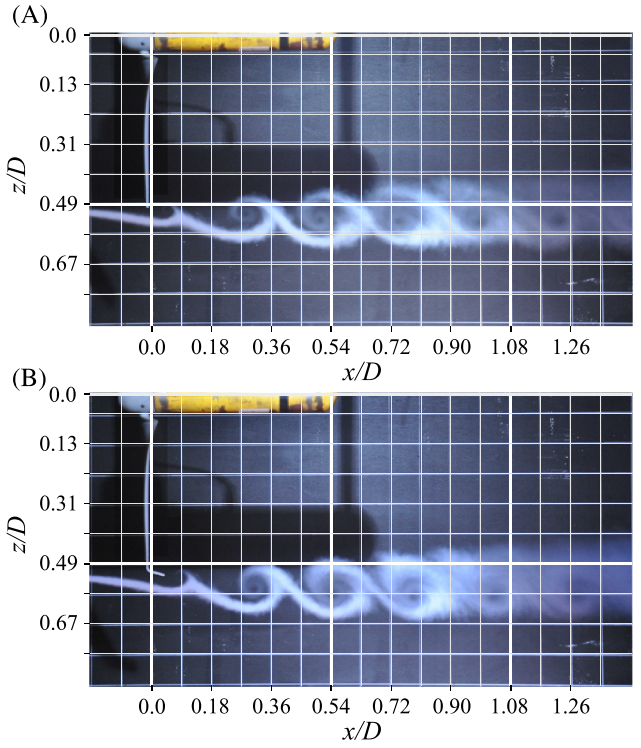

FIGURE 6 Smoke visualization of the tip vortex path for A, rotor without winglets and B, rotor with winglets [Colour figure can be viewed at wileyonlinelibrary.com]

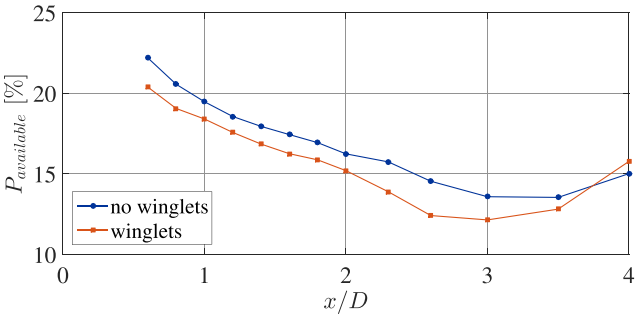

FIGURE 7 Available power for an imaginary downstream rotor in the wake in percent of total available energy [Colour figure can be viewed at wileyonlinelibrary.com]

as depicted in Figure 8B. This observation will be quantified in detail in Section 3.3, where the normal and shear stress components are analyzed in line plots for different sections of the wake (Figures 9 and 10).

The peak levels of total kinetic energy between $x/D = 0.3$ - 2.0 are assessed to be of comparable magnitude for both cases. A slightly higher total kinetic energy measured for the wingletted configuration indicates an insignificantly stronger tip vortex in this case. As previously observed in the evaluation of the mean streamwise velocity, the wake seems to be slightly broader for the wingletted case, which is confirmed by a slight lateral offset in z-direction of the kinetic energy peaks. At the downstream distances $x/D = 2.3$ and 2.6, however, the total kinetic energy peak shape significantly deviates. While the total kinetic energy seems to be concentrated in a single peak for the nonwingletted reference case, a significantly broader double peak develops for the wingletted configuration at these two downstream distances. The peak levels are seen to be smaller for the winglet case, while the energy seems to be distributed in a broader peak. At even higher downstream distances from $x/D \geq = 3.0$, the two peaks melt into a single peak again, showing a very similar distribution as measured for the reference case again. The levels of total kinetic energy are measured to be very similar for the both configurations at these locations. As this is a rather qualitative description of the mean total kinetic energy so far, a closer look into the single components of the turbulent stress tensor will be given in Section 3.3. An analysis of the phase-averaged quantities and the interaction mechanisms will thereafter be given in Section 3.4.

3.3 | The stress tensor

For a better understanding of the underlying mechanisms, the streamwise development of the three normal stresses $\overline{u_x u_x}$, $\overline{u_y u_y}$ and $\overline{u_z u_z}$ is further analyzed in Figure 9. Note that the scale changes between the single measurement stations. Up until a downstream distance of $x/D = 2.0$, the normal stresses are concentrated to a narrow region around $z/D = 0.55$ for the reference configuration and $z/D = 0.60$ for the wingletted configuration, respectively. Up to a downstream distance of about $x/D = 2.0$, the vertical normal stress $\overline{u_y u_y}$ component has the highest magnitude of the three normal stress components. For both tip configurations, the spanwise normal stress $\overline{u_z u_z}$ initially has the lowest magnitude, reaching a similar magnitude as the streamwise stress at $x/D = 2.0$. As already observed in the analysis of the total kinetic energy, significant deviations

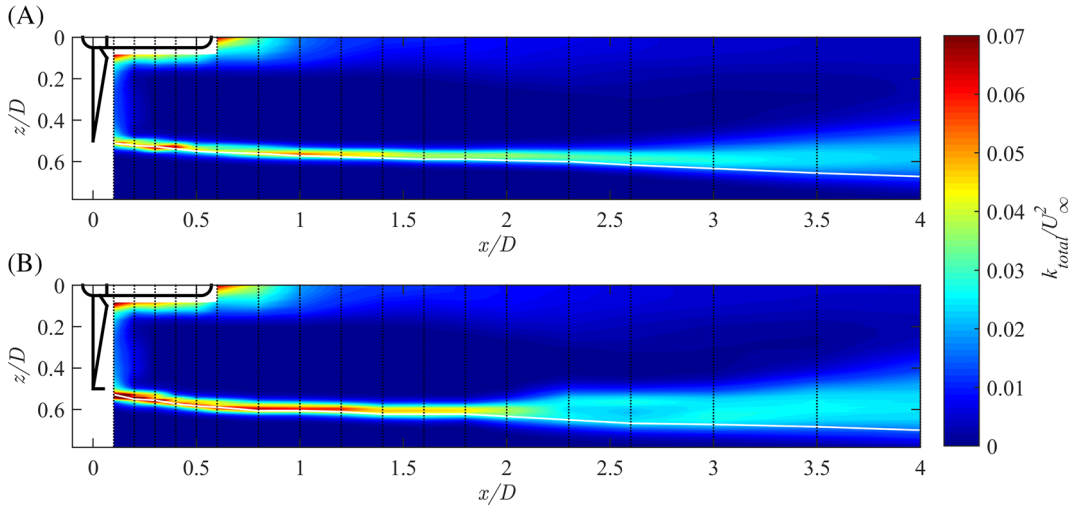

FIGURE 8 Total kinetic energy for the rotor configuration A, without winglets and B, with winglets. The white lines indicate locations of $\overline{U_x}/U_\infty = 1$ [Colour figure can be viewed at wileyonlinelibrary.com]

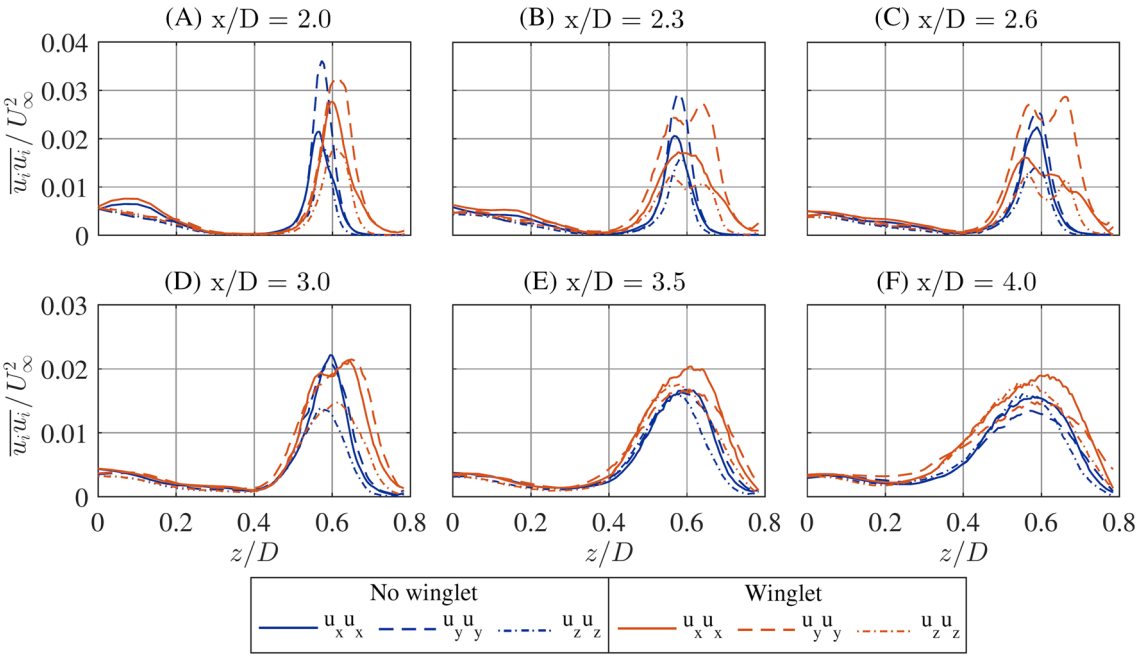

FIGURE 9 Horizontal profiles of the normal stresses $\overline{u_i u_i}/U^2_\infty$ at selected downstream distances x/D for a nonwingletted and wingletted configuration. Note that the scale of the normal stress range changes [Colour figure can be viewed at wileyonlinelibrary.com]

between the two rotor tip configurations occur around x/D = 2.3 - 2.6. While the peaks of the reference configuration approximately keep their width, all three peaks of the wingletted configuration become significantly broader at x/D = 2.3. A bimodal peak for the vertical and spanwise normal stresses $\overline{u_y u_y}$ and $\overline{u_z u_z}$ is measured, while the streamwise stress $\overline{u_x u_x}$ continues to feature one distinct peak only. The bimodal peak shape is due to the two tip vortices interacting in this region, as an analysis of the phase-averaged quantities in the next section will reveal. At the same time, the vortex centers are slightly displaced in spanwise direction. The bimodal peak is then merging into a single peak at x/D = 3.0 - 4.0 again, while the peaks for all three components are seen to be broader than for the reference configuration. In this region, the vortices begin to break up into turbulent structures as will be explained in the next chapter. In the wake behind the nonwingletted reference rotor, no mutual interaction of the tip vortices is detected in the region between x/D = 2.3 - 2.6, while the kinetic energy is gradually transferred from the vertical stress $\overline{u_y u_y}$ to the streamwise $\overline{u_x u_x}$ and spanwise $\overline{u_z u_z}$ stresses, respectively. For both rotor configurations, the vertical stresses $\overline{u_y u_y}$ dominate the tip region of the wake up until x/D = 2.6. At x/D = 3.0 already, the streamwise stresses $\overline{u_x u_x}$ contain just as much energy as the vertical ones. At x/D = 4.0, the streamwise and spanwise stresses $\overline{u_x u_x}$ and $\overline{u_z u_z}$ are very similar, while the earlier dominating vertical stresses contain less energy. From x/D = 4.0 the shear layer is dominated by diffusive mechanisms for both blade tip configurations. From this location, the distribution of the total kinetic energy is more isotropic, although this only counts as a rough approximation.

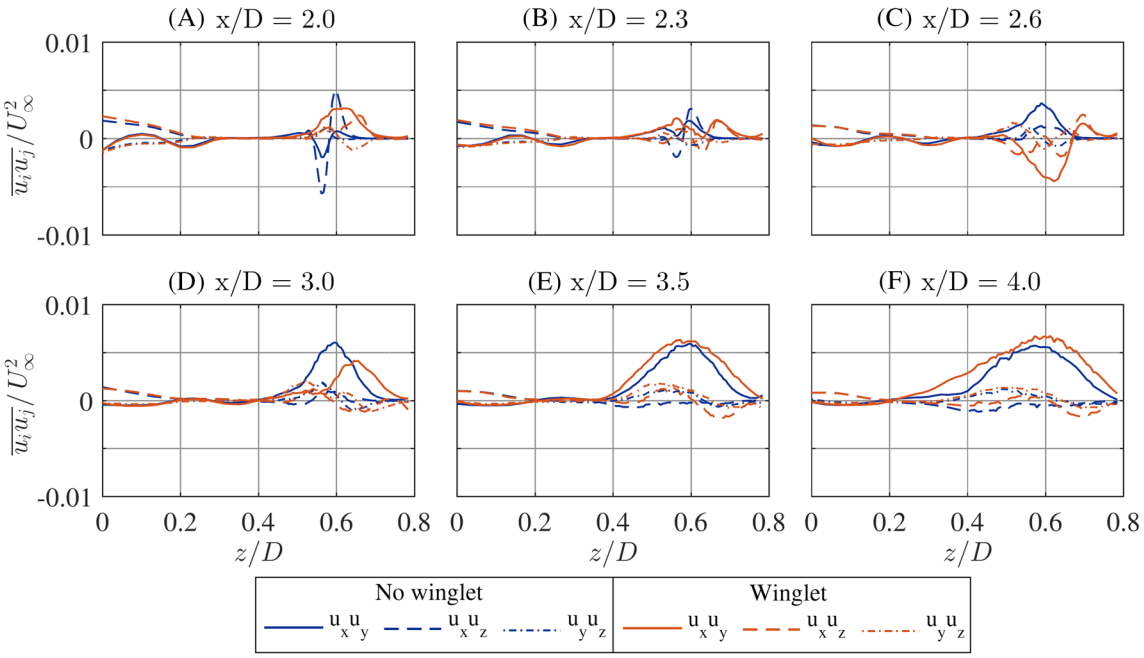

FIGURE 10 Horizontal profiles of the shear stresses $\overline{u_i u_j}/U_\infty^2$ at selected downstream distances x/D for a nonwingletted and wingletted configuration [Colour figure can be viewed at wileyonlinelibrary.com]

Similarly, increased shear stresses are found in the shear layer generated by the path of the tip vortices as shown in Figure 10. These shear stresses $\overline{u_i u_j}$ play a dominant role in the production of turbulent kinetic energy. Approximately, the same spanwise displacement as for the normal stresses is assessed for the wingletted configuration. The first significant differences between the two configurations can be detected at $x/D = 2.0$. Both $\overline{u_x u_y}$ and $\overline{u_x u_z}$ have a purely positive contribution for the wingletted case, while both shear stresses feature a change of sign from negative to positive around the vortex core for the straight wing tip configuration. The interaction of two tip vortices behind the winglet blade tip is again detected in a bimodal peak of the $\overline{u_x u_y}$ term at $x/D = 2.3$, which then transforms into a bimodal negative peak of the $\overline{u_x u_z}$ term at $x/D = 2.6$. The vortex interaction behind the wingletted rotor seems to be completed at $x/D = 3.0$, while the strong vortex cores behind the straight wing tip simply seem to have decayed at this downstream distance. In both cases, the shear layer is now dominated by the $\overline{u_x u_y}$ stress, while the other shear stresses are seen to flatten out. The shear layers are observed to broaden out at $x/D = 4.0$ as previously seen for the normal stresses.

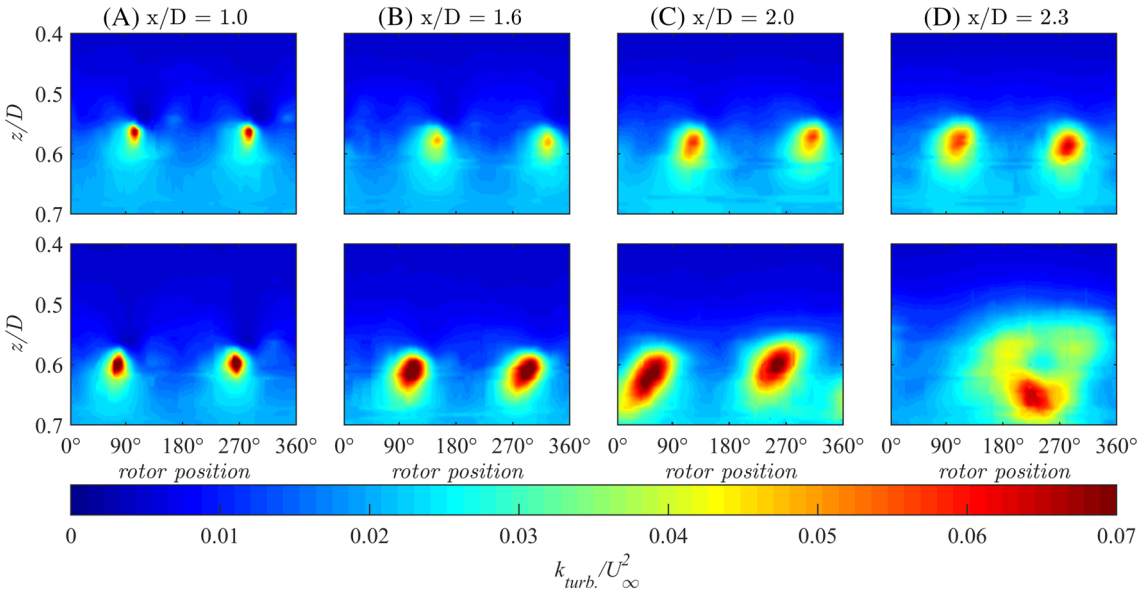

FIGURE 11 Phase-averaged turbulent kinetic energy k_{turb}/U_∞^2 at A, $x/D = 1.0$, B, $x/D = 1.6$, C, $x/D = 2.0$, and D, $x/D = 2.3$ for all rotor positions 0°-360°. Upper row: No winglet reference case. Lower row: Winglet case [Colour figure can be viewed at wileyonlinelibrary.com]

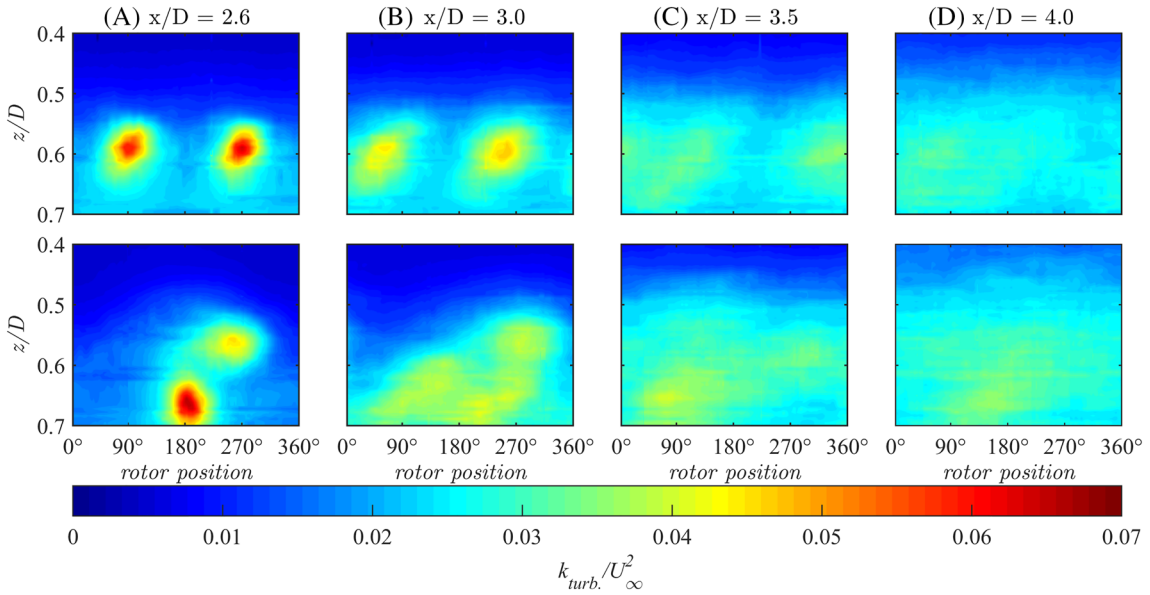

FIGURE 12 Phase-averaged turbulent kinetic energy k_{turb}/U_∞^2 at A, $x/D = 2.6$, B, $x/D = 3.0$, C, $x/D = 3.5$, and D, $x/D = 4.0$ for all rotor positions 0°-360°. Upper row: No winglet reference case. Lower row: Winglet case [Colour figure can be viewed at wileyonlinelibrary.com]

3.4 | Phase-averaged kinetic energy

So far, we have only discussed time-averaged quantities describing the mean flow conditions. As the sampling of the wake flow was synchronized with the rotor position, conditional averaging allows us to assign the measured values to a rotor phase. Thus, we can identify the turbulent kinetic energy and vorticity contained in the individual vortical structures at the different downstream locations for both rotor configurations. At first, the phase-averaged turbulent kinetic energy in the wake behind the two rotor configurations is compared in Figure 11 for $x/D = 1.0$ - 2.3 and Figure 12 for $x/D = 2.6$ - 4.0, respectively. Note that the initial tip vortices might not appear completely round as the axes have different units, ie, a nondimensional length and the rotor's azimuth angle, respectively. In case of the nonwingletted reference configuration, as depicted in the upper row, the vortex cores are gradually moving outwards to higher z/D with increasing downstream distance x/D. A similar trend is observed for the wingletted configuration depicted in the lower rows of Figures 11 and 12. At about $x/D = 1.6$, the vortices behind the wingletted rotor are assessed to grow significantly stronger than the vortices behind the nonwingletted reference rotor. Between $x/D = 2.0$ and $x/D = 2.3$, the two tip vortices start interacting behind the wingletted rotor configuration, while no interaction is seen for the vortices behind the nonwingletted rotor. At $x/D = 2.6$ one of the two vortex cores behind the wingletted configuration is seen to transport significantly less turbulent kinetic energy than the other vortex core. The weaker vortex is deflected inwards and wrapped around the stronger vortex core. The vortex pairing is observed to happen between $x/D = 2.3$ and $x/D = 2.6$ behind the wingletted rotor, while the vortices shed from the straight-cut rotor are not observed to pair in this downstream region yet. At $x/D = 3.0$, no explicit vortex cores can be detected anymore, while the turbulent kinetic energy is more evenly distributed over the whole range of rotor phases. In contrast to that, the vortex cores behind the nonwingletted reference rotor are not seen to significantly interact for the measured range of downstream distances up to $x/D = 4.0$. In the interesting part of downstream range between $x/D = 2.0$ and $x/D = 3.0$, the vortex cores kept their lateral position, while the transported turbulent kinetic energy in the vortices is gradually decaying without any significant interaction between the vortices. At $x/D = 4.0$, the turbulent kinetic energy is evenly distributed for both rotor tip configurations. In both cases, the energy contained in the periodic motions has at this point almost completely transferred to fully developed turbulent motions.

3.5 | Phase-averaged vorticity

The interaction of the tip vortices behind the different rotor configurations is further investigated by an analysis of the phase-averaged out-of-plane vorticity component $\langle\omega_y\rangle = \langle\partial u_x/\partial z - \partial u_z/\partial x\rangle$. Since the vortices are traveling downstream in the shear layer, the streamwise convective velocity U_{conv} has to be subtracted to calculated the local vorticity. Thus, the time derivatives can be transformed to spatial derivatives using Taylor frozen equilibrium approximation $\Delta x \approx U_{conv}\Delta\tau$. Therein, U_{conv} is approximated from the local mean velocity at the inner border of the shear layer between z/D=0.5-0.6. As the wake of the wingletted rotor is observed to be slightly broader the local velocities between z/D=0.5-0.6 are smaller, leading to slight differences in the convective speed approximation.

The results of the phase-averaged vorticity $\langle\omega_y\rangle$ approximations downstream of the two rotor configurations are compared in Figure 13 for $x/D = 1.0$ - 2.3 and Figure 14 for $x/D = 2.6$ - 4.0, respectively. The blue arrows indicated the approximated velocity vectors in the xz-plane, while the color scale visualizes the strength of the out-of-plane vorticity. Note that the color scale changes from Figure 13 to 14. Apart from the previously discussed lateral offset of the tip vortices in the wingletted case, the development of the vorticity $\langle\omega_y\rangle$ up to $x/D < 2.0$ is observed

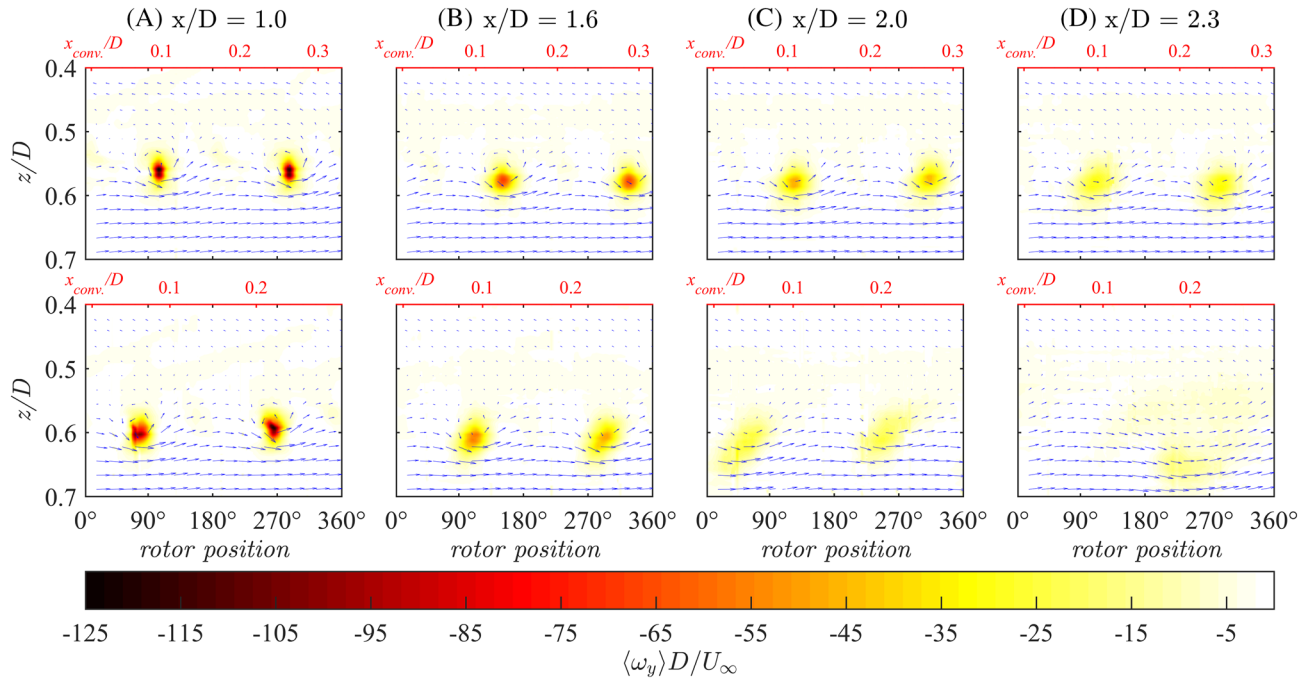

FIGURE 13 Normalized phase-averaged out-of-plane vorticity $\langle\omega_y\rangle D/U_\infty$ at A, $x/D = 1.0$, B, $x/D = 1.6$, C, $x/D = 2.0$, and D, $x/D = 2.3$ for all rotor positions 0°-360°. Upper row: No winglet reference case. Lower row: Winglet case [Colour figure can be viewed at wileyonlinelibrary.com]

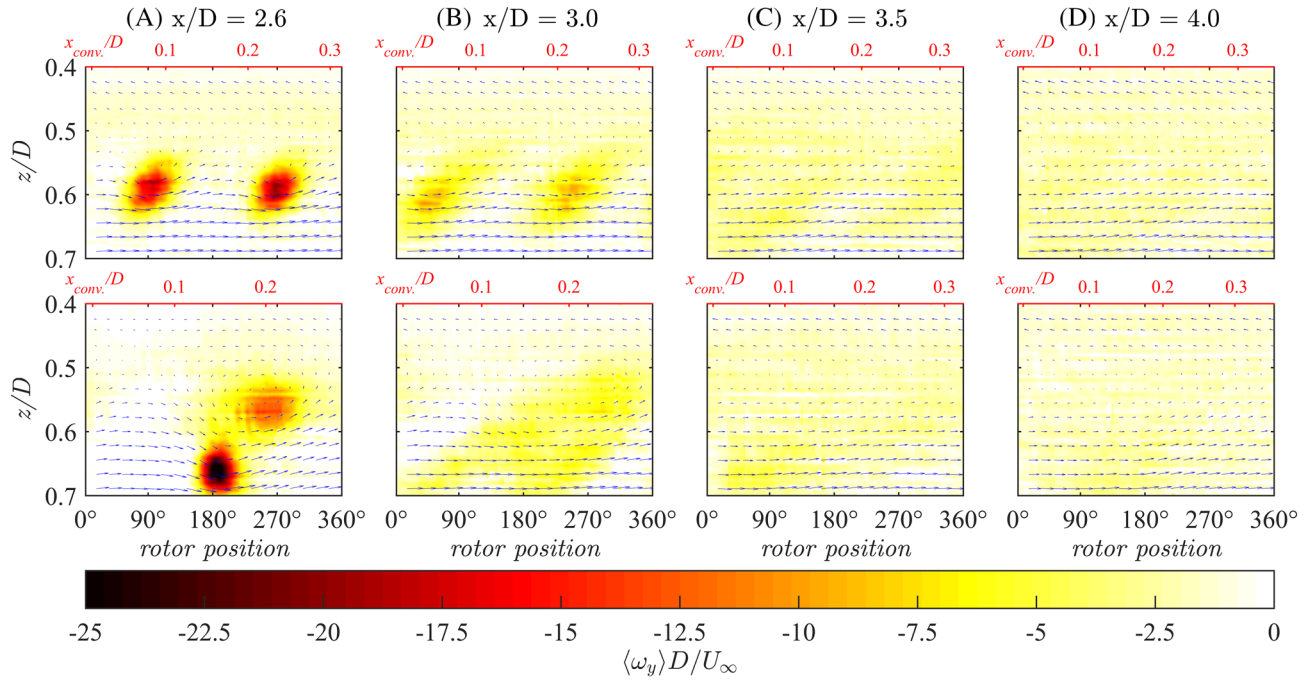

FIGURE 14 Normalized phase-averaged out-of-plane vorticity $\langle\omega_y\rangle D/U_\infty$ at A, $x/D = 2.6$, B, $x/D = 3.0$, C, $x/D = 3.5$, and D, $x/D = 4.0$ for all rotor positions 0°-360°. Upper row: No winglet reference case. Lower row: Winglet case [Colour figure can be viewed at wileyonlinelibrary.com]

to be very similar for both rotor configurations. A significant difference in the vorticity between the two configurations is detected at $x/D = 2.0$. The vorticity behind the wingletted rotor is observed to be diagonally spread along $x = z$, while the vorticity behind the reference rotor is still concentrated in a circular core. At $x/D = 2.3$ only one defined vortex core is detected for the wingletted configuration. The second vortex is seen to strongly interact with the first vortex at $x/D = 2.6$, riding on top of each other before finally merging into a single structure at $x/D = 3.0$. In contrast to that, evenly spaced vortex cores are still detected for the reference configuration at $x/D = 2.6$ and 3.0. A slight interaction of two significantly weaker and more spread out vortices is suspected to happen at $x/D = 3.5$ for the reference configuration, while the largest portion of the vorticity has already decayed. At $x/D = 4.0$, the phase-averaged vorticity $\langle\omega_y\rangle$ is assessed to be evenly distributed over the entire range of rotor positions for both investigated blade tip configurations, indicating completely decayed tip vortices to a turbulent shear layer.

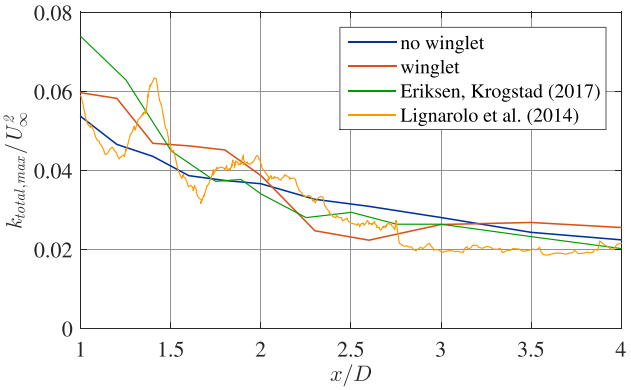

FIGURE 15 Streamwise decay of time-averaged total kinetic energy levels $k_{total,max}/U_\infty^2$ for the two blade tip configurations. Reference data measured behind a three-bladed nonwingletted rotor by Eriksen and Krogstad[17] and a two-bladed rotor by Lignarolo et al[16] [Colour figure can be viewed at wileyonlinelibrary.com]

4 | DISCUSSION

The results of the study revealed a number of significant differences in vorticity and turbulent kinetic energy contained in the tip vortices behind the two different blade tip configurations. A previous investigation on the same rotor configurations by Hansen and Mühle[9] disclosed significant differences of the flow in the tip region on the blade's suction side. In this region, the winglet forced the flow to be more parallel in chordwise direction on the suction side of the blade, reducing the amount of spanwise flow as observed for the nonwingletted reference case. Thus, the induced drag could be reduced by the winglets, leading to an increased power extraction and a higher thrust coefficient for the wingletted rotor. The measurement of the wake flow was assessed to be restricted due to very high flow angles in the tip vortex region up to a downstream distance of about $x/D = 1.0$. As the cobra probe's operating range is limited to flow angles up to $\theta \leq 45°$, this resulted in a considerable reduction of the evaluated data in the tip vortex region up to $x/D = 1.0$. The reduced data might not depict the real vortices as the high flow angles are not resolved. For downstream distances $x/D \geq 1.0$, however, the major part of the acquired data is deemed to be reliable. The time-averaged mean streamwise flow is generally seen to compare well for both blade tip configurations, while the only significant difference is a wider initial wake extension after the wingletted rotor. This finding agrees well with earlier observations by Shimizu et al,[25] Johansen and Sørensen,[5] Tobin et al,[12] and Ostovan et al.[11] Ostovan et al.[11] also measured a wider wake extension and thicker mixing layer in the very near wake behind a three-bladed wingletted rotor. A closer look into the fluctuating quantities in the wake revealed significant differences between the two investigated configurations. An evaluation of the normal and shear stresses showed a strong deviation between the two blade tip configurations of these quantities for the downstream distances $x/D = 2.3$ - 2.6. A detailed investigation of the phase-averaged turbulent kinetic energy k_{turb}/U_∞^2 as well as the out-of-plane vorticity $\langle\omega_y\rangle D/U_\infty$ indicated a strong interaction of the tip vortices behind the wingletted rotor tip configuration and, as a consequence, a shear layer enlargement within this downstream range. Simultaneously, the tip vortices measured behind the nonwingletted reference configuration kept their position with little visible interaction. An interaction of the significantly weaker vortices could be suspected around $x/D \approx 3.5$ for the straight cut wing tip. At $x/D = 4.0$, the turbulent kinetic energy and vorticity distributions were also observed to be very similar for both configurations. At this downstream distance, the tip vortices have almost completely broken up into purely turbulent motions for both rotor configurations, indicated by an evenly spread vorticity over the entire measurement window. The peak levels of the time-averaged total kinetic energy measured in the wake behind both rotors are compared in Figure 15 for all downstream distances $x/D = 1.0$ - 4.0. The peak levels are assessed to be higher for the winglet case for all downstream distances up to $x/D = 2.0$, due to a stronger loading of the wingletted rotor in the tip region. At $x/D = 2.3$ and 2.6, the kinetic energy peak levels behind the winglet tips are lower, as the vortical structures were observed to interact in this downstream region. From about $x/D = 3.0$, the levels of peak kinetic energy were assessed to be very similar for both tip configurations, being more and more dominated by purely turbulent motions.

The decay of the total kinetic energy is furthermore compared with two reference data sets measured downstream of two nonwingletted rotors by Eriksen and Krogstad[17] and Lignarolo et al[16] in Figure 15. It is observed that the decay of the time-averaged total kinetic energy is generally comparable with both reference data sets. A slightly higher initial $k_{total,max}$ at $x/D = 1.0$ measured by Eriksen and Krogstad[17] can be

TABLE 3 Comparison of rotor tip design, inflow parameters, and location of vortex interaction with reference studies by Eriksen and Krogstad[17] and Lignarolo et al[16]

	Rotor Diameter, m	No. of Blades N_B	Tip Airfoil	Tip chord Length, mm	Rotor C_T (–)	Inflow TI, %	Vortex Interaction (x/D)
Mühle et al							
Reference	0.90	2	R-opt	39.7	0.87	0.23	≈ 3.5
Mühle et al							
Winglets	0.90	2	W-opt	20.2	0.98	0.23	2.3-2.6
Eriksen and							
Krogstad	0.90	3	NREL S826	26	0.89	0.24	1.75-2.5
Lignarolo et al	0.60	2	Eppler E387	44	0.88	0.50	1.5

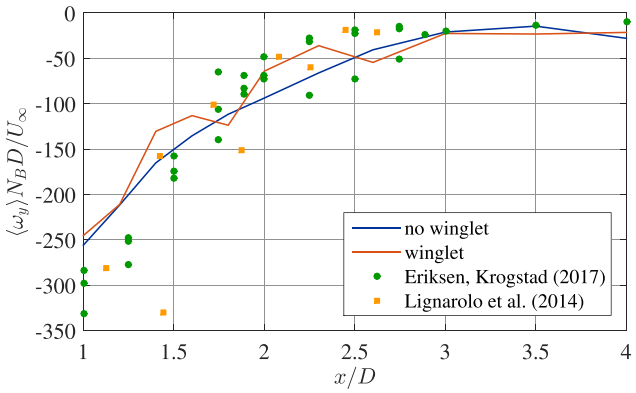

FIGURE 16 Comparison of the streamwise development of peak vorticity levels $\langle\omega_y\rangle N_B D/U_\infty$ for the two blade tip configurations. Peak vorticity levels are extracted from the vortex center of the stronger of the two vortices. Reference data of the three individual vortices behind a three-bladed nonwingletted rotor by Eriksen and Krogstad[17] and the two individual vortices behind a two-bladed rotor by Lignarolo et al[16] [Colour figure can be viewed at wileyonlinelibrary.com]

explained by an additional tip vortex shed off their three-bladed rotor, which is operated at the same tip speed ratio $\lambda = 6.0$. The peak total kinetic energy derived from PIV measurements by Lignarolo et al[16] behind a two-bladed rotor operated at $\lambda = 6.0$ is also seen to decay similarly as in the presented data set. In both reference experiments, the rotors are designed with straight cut-off blade tips featuring a comparable tip chord length as in the present experiment. Lignarolo two-bladed rotor features a tip chord length of $L_{c,tip} = 44$ mm, while Eriksen and Krogstad rotor is three-bladed with a tip chord length of $L_{c,tip} = 26$ mm. The main parameters defining the rotor tip design, inflow conditions, and downstream location of vortex interaction are compared in Table 3. Comparing the decay of total kinetic energy in the wake of a two- and three-bladed rotor, it seems that the initially higher energy levels approximate around $x/D = 2$. Even further downstream, the marginally higher energy levels are found behind the blade tips of a two-bladed rotor, comparing the blue (Mühle et al, "no winglets") and green (Eriksen and Krogstad) curve. This is in agreement with studies on the effect of blade numbers on the time-averaged wake flow by Mühle et al[26] and Bartl et al,[27] in which higher turbulent kinetic energy levels are found for a two-bladed rotor than for a three-bladed rotor from $x/D \geq 3$.

A comparison of the streamwise development of the peak vorticity levels $\langle\omega_y\rangle N_B D/U_\infty$ extracted from the stronger of the two vortex cores is presented in Figure 16. Herein, N_B denotes the number of blades on the rotor and D the rotor diameter. Note the negative sign in the vorticity scale when comparing absolute vorticity levels. The absolute value of the peak vorticity is assessed to be higher for the nonwingletted reference configuration up to a downstream distance of approximately $x/D = 2.6$, while very similar vorticity levels are measured for $x/D = 2.6$ - 4.0. This is in agreement with results from Ostovan et al,[11] who measured larger but weaker vortices in the very near wake behind a wingletted blade tip. The lower absolute vorticity levels measured at $x/D = 2.0$ - 2.6 behind the winglet rotor can be explained by the mutual induction of the two tip vortices observed in this downstream region. The reference data set by Eriksen and Krogstad[17] marked with the green dots in Figure 16 initially shows significantly higher absolute vorticity levels extracted from the three individual vortex cores. The three vortices were seen to interact in a downstream region between $x/D = 1.75$ - 2.5, which is significantly further upstream than for both configuration of the two-bladed rotor used in this study. As three vortices are shed in Eriksen and Krogstad experiment instead of two in the present study over a very similar convective length, the spacing between the individual vortices is about 1.5 times tighter behind the three-bladed rotor, leading to an earlier vortex interaction. Considerably higher initial absolute vorticity levels have also been extracted from the vortex cores in the PIV experiment by Lignarolo et al[16] as indicated by the orange dots in Figure 16. As in the present study, Lignarolo et al used a two-bladed rotor operated at a similar thrust coefficient $C_T = 0.88$ and tip speed ratio $\lambda = 6.0$. In their experiment, an initial vortex interaction was however already detected at $x/D = 1.5$. Their straight cut blade tips with a chord length of $L_{c,tip} = 44$ mm were only insignificantly longer than for the rotor used in the present study ($L_{c,tip} = 39.7$ mm). The exact reasons for a much earlier tip vortex interaction in Lignarolo et al experiment are not completely known. The increased level in inflow turbulence intensity $TI_{Inflow,Delft} = 0.50\%$ compared with $TI_{Inflow,Trondheim} = 0.23\%$ in the present experiment, however, is deemed to be an important influence factor. The higher inflow turbulence might have triggered an instability earlier, which could have caused the tip vortices to interact already at a significantly smaller downstream distance.

5 | CONCLUSIONS

An experimental study on the effect of winglets on the vortex interaction and breakup in the wake of a model wind turbine is presented. The mean streamwise velocity in the near wake region up to $x/D = 4.0$ is found not to be significantly affected by the presence of the winglets, although a previous study by Hansen and Mühle[9] assessed a 7.8%-8.9% higher power coefficient of the wingletted rotor compared with the reference setup. This result indicates that winglets do not negatively affect the mean kinetic energy in the wake flow as a one-dimensional energy conservation law would suggest. The downstream-facing winglets create a slightly wider wake compared with a nonwingletted reference rotor, while the mean velocity field otherwise is very similar. An investigation of the total kinetic energy, comprising the energy contained in the coherent and the turbulent motions of the tip vortices, reveals slightly higher initial peaks in the tip region for a wingletted tip configuration. In a downstream range between $x/D \approx 2.0$ and 3.0, the shear layer behind the tip region is observed to be significantly broader for the wingletted configuration, indicated by bimodal peaks in two of the normal stresses at $x/D = 2.3$ and 2.6. An analysis of the phase-averaged out-of-plane

vorticity component indicates an instability in this region, causing the tip vortices to interact before entirely breaking up around $x/D \approx 3.0$. In contrast to that, no interaction of the tip vortices behind the straight-cut reference tips is detected before $x/D \approx 3.5$, where the two significantly weaker tip vortices started to merge. Considering the application of winglets on multiple rotors in a wind farm setup, the presented results indicate that a higher power extraction in a wingletted rotor's tip region can also positively affect the wake's mean kinetic energy recovery by stimulating a faster tip vortex interaction. Thus, winglets might not only positively affect the power output of a single turbine but also mitigate wake losses.

6 | DATA AVAILABILITY STATEMENT

All data of the experimental setup (airfoil geometry, blade geometry, turbine geometry, and wind tunnel geometry) as well as the results of the wake measurements (time-averaged and phase-averaged quantities) presented in this paper are publicly available at https://doi.org/10.5281/zenodo.3310799 (Mühle et al.[28]).

NOMENCLATURE

Geometrical measures	
D	[m] Rotor diameter
x/D	[-] Streamwise location as a multiple of the rotor diameter
z/D	[-] Lateral location as a multiple of the rotor diameter
$L_{c,tip}$	[m] Chord length at the blade tip
Rotor features	
N_B	[-] Number of blades on the rotor
C_P	[-] Rotor power coefficient
C_T	[-] Rotor thrust coefficient
λ	[-] Rotor tip speed ratio
Inflow conditions	
U_∞	[m/s] Inlet velocity (measured x/D=2.0 upstream of the rotor)
TI	[%] Inlet turbulence intensity level at rotor position
Flow parameters in the wake	
$U_i(t) = U_i + \tilde{u}_i + u_i'$	[m/s] Triple decomposition of the velocity time series
$u_i(t) = \tilde{u}_i + u_i'$	[m/s] Decomposition of the fluctuating part of the time series
U_i	[m/s] Mean velocity component (i = [x, y, z])
$k_{total} = \sum_i \tilde{u}_i\tilde{u}_i + \sum_i u_i'u_i'$	$[m^2/s^2]$ Total (periodic and turbulent) kinetic energy
$k_{turb} = \sum_i u_i'u_i'$	$[m^2/s^2]$ Turbulent kinetic energy
$\tilde{u}_i\tilde{u}_i$	$[m^2/s^2]$ Periodic kinetic energy component (i = [x, y, z])
$u_i'u_i'$	$[m^2/s^2]$ Turbulent kinetic energy component (i = [x, y, z])
u_iu_i	$[m^2/s^2]$ Total normal stress component (i = [x, y, z])
u_iu_j	$[m^2/s^2]$ Total shear stress component ([i, j] = [x, y, z])
U_{conv}	$[m/s]$ Estimated convective velocity of the tip vortices
θ	[°] Flow angle
ω_y	[1/s] Out of plane (xz-plane) vorticity
P	$[W/m]$ Available power for an imaginary downstream rotor
A_i	$[m]$ Segment length of measured wake profile
ρ	$[kg/m^3]$ Air density
Mathematical operators	
$\bar{a}$	Time-average of quantity a
$\langle a \rangle$	Phase-average of quantity a
$\partial a/\partial x$	Partial derivation of quantity a with respect to x

ORCID

Jan Bartl https://orcid.org/0000-0002-1580-0882
Thomas Hansen https://orcid.org/0000-0003-4048-804X

REFERENCES

1. van Dam CP, Holmes BJ, Pitts C. Effect of winglets on performance and handling qualities of general aviation aircraft. *J Aircr*. 1981;18:587-591.
2. Eppler R. Induced drag and winglets. *Aerosp Sci Technol*. 1997;1(1):3-15.
3. Faye R, Laprete R, Winter M. Blended winglets for improved airplane performance. *Aero Mag*. 2002;17:16-31. http://www.boeing.com/commercial/aeromagazine/aero_17/winglet_story.html
4. Giuni M, Green RB. Vortex formation on squared and rounded tip. *Aerosp Sci Technol*. 2013;29:191-199.
5. Johansen J, Sørensen NN. Aerodynamic investigation of winglets on wind turbine blades using cfd. https://core.ac.uk/download/pdf/13776041.pdf, ISSN 0106-2840; 2006.
6. Johansen J, Sørensen NN. *Numerical analysis of winglets on wind turbine blades using cfd*: European Wind Energy Congress; 2007.
7. Gaunaa M, Johansen J. Determination of the maximum aerodynamic efficiency of wind turbine rotors with winglets. *J Phys: Conf Ser*. 2007;75(1):012006.
8. Gertz D, Johnson DA, Swytink-Binnema N. An evaluation testbed for wind turbine blade tip designs—winglet results. *Wind Eng*. 2012;36(4):389-410.
9. Hansen TH, Mühle F. Winglet optimization for a model-scale wind turbine. Wind Energy; 2018.
10. Ostovan Y, Uzol O. Experimental study on the effects of winglets on the performance of two interacting horizontal axis model wind turbines. *J Phys Conf Ser*. 2016;753(2):022015.
11. Ostovan Y, Akpolat M, Uzol O. Experimental investigation of the effects of winglets on the tip vortex behavior of a model horizontal axis wind turbine using particle image velocimetry. *J Solar Energy Eng*. 2018;141(1):011006.
12. Tobin N, Hamed AM, Chamorro LP. An experimental study on the effects ofwinglets on the wake and performance of a modelwind turbine. *Energ*. 2015;8(10):11955-11972.
13. Sørensen JN. Instability of helical tip vortices in rotor wakes. *J Fluid Mech*. 2011;682:1-4.
14. Sarmast S, Dadfar R, Mikkelsen RF, Schlatter P, Ivanell S, Sørensen JN, Henningson DS. Mutual inductance instability of the tip vortices behind a wind turbine. *J Fluid Mech*. 2014;755:705-731.
15. Okulov VL, Kabardin IK, Mikkelsen RF, Naumov IV, Sørensen JN. Helical self-similarity of tip vortex cores. *J Fluid Mech*. 2019;859:1084-1097.
16. Lignarolo LEM, Ragni D, Krishnaswami C, Chen Q, Simao Ferreira CJ, van Bussel GJW. Experimental analysis of the wake of a horizontal-axis wind-turbine model. *Renew Ener*. 2014;70:31-46.
17. Eriksen P-E, Krogstad P. Development of coherent motion in the wake of a model wind turbine. *Renew Energy*. 2017;108:449-460.
18. Bastankhah M, Porté-Agel F. Wind tunnel study of the wind turbine interaction with a boundary-layer flow: upwind region, turbine performance, and wake region. *Phys Fluids*. 2017;29:065105.
19. Shepherd IC. A four hole pressure probe for fluid flow measurements in three dimensions. *J Fluid Eng*. 1981;103(4):590-594.
20. Hooper JD, Musgrove AR. Reynolds stress, mean velocity, and dynamic static pressure measurement by a four-hole pressure probe. *Exp Thermal Fluid Sci*. 1997;15(4):375-383.
21. Wheeler AJ, Ganji AR. *Introduction to Engineering Experimentation*. Third edition: Upper Saddle River, NJ, USA, Pearson/Prentice Hall, XI; 2004.
22. Benedict L, Gould R. Towards better uncertainty estimates for turbulence statistics. *Exper Fluids*. 1996;22:129-136.
23. Bartl J, Mühle F, Schottler J, et al. Wind tunnel experiments on wind turbine wakes in yaw: effects of inflow turbulence and shear. *Wind Energ Sci*. 2018;3:329-343.
24. Cantwell B, Coles D. An experimental study of entrainment and transport in the turbulent near wake of a circular cylinder. *J Fluid Mech*. 1983;136:129-136.
25. Shimizu Y, Imamura H, Matsumura S, Maeda T, van Bussel GJW. Power augmentation of a horizontal axis wind turbine using a mie type tip vane: velocity distribution around the tip of a hawt blade with and without a mie type tip vane. *ASME J Solar Energy Eng*. 1995;117:297-303.
26. Mühle F, Adaramola M, Sætran L. The effect of the number of blades on wind turbine wake—a comparison between 2-and 3-bladed rotors. *J Phys Conference Series*. 2016;753(3):032017.
27. Bartl J, Hansen T, Kuhn WL, Mühle F, Sætran L. Vortex interaction in the wake of a two- and three-bladed wind turbine rotor. *J Phys Conference Series (in review)*. 2020.
28. Mühle F, Bartl J, Hansen T. Wake data documentation for a wind turbine rotor with winglets. *Zenodo online database*. 2019.

How to cite this article: Mühle F, Bartl J, Hansen T, Adaramola MS, Sætran L. An experimental study on the effects of winglets on the tip vortex interaction in the near wake of a model wind turbine. *Wind Energy*. 2020;23:1286–1300. https://doi.org/10.1002/we.2486